Hindawi
Journal of Spectroscopy
Volume 2019, Article ID 9191328, 10 pages
https://doi.org/10.1155/2019/9191328

Research Article

Vibrational Fingerprint of Erlotinib: FTIR, RS, and DFT Studies

Natalia Piergies, Czesława Paluszkiewicz, and Wojciech M. Kwiatek

Institute of Nuclear Physics Polish Academy of Sciences, PL-31342 Krakow, Poland

Correspondence should be addressed to Natalia Piergies; natalia.piergies@ifj.edu.pl

Received 21 March 2019; Revised 18 June 2019; Accepted 30 July 2019; Published 20 August 2019

Academic Editor: Pedro D. Vaz

In this study, we provide the first Fourier-transform infrared absorption spectroscopy (FTIR) and Raman spectroscopy (RS) analysis of a vibrational fingerprint of erlotinib, a drug which is applied in non-small cell lung cancer therapy, in solid state and solution in different pH conditions. Additionally, the performed DFT theoretical calculations in vacuum and PCM models support the interpretation of vibrational spectra and give insight into an optimized spatial configuration of the investigated drug. The present considerations show vibrational structure of erlotinib and details of its molecular geometry. Furthermore, we discuss the pH condition where the protonated $-NH^+$ and $C=N^+$ forms occur and indicate the spectral changes characteristic for the erlotinib protonation. It is of great of importance to better understand biological activity of the drug and to develop new tyrosine kinase inhibitors.

1. Introduction

In the last few decades, scientific research focused on understanding tumor formation [1–4]. Studies have shown that an accumulation of genetic and epigenetic mutations is one of the most serious factors promoting cancer disease [1, 2]. Therefore, there is a great interest in creating extremely sensitive and specific drugs that could be used in cancer therapy. Erlotinib, known also as TARCEVA (see Figure 1 for molecular structure), is one of the drugs with particular activity against epidermal growth factor receptor (EGFR) activation [5]. Overexpression of EGFR is observed in 50% of non-small cell lung cancers (NSCLCs). This tyrosine kinase inhibitor competes with adenosine triphosphate (ATP) for the binding side of EGFR, prevents the tyrosine phosphorylation, and thus blocks signaling pathway in the target cell. Erlotinib is applied in NSCLC therapy for patients with recognized EGFR-activating mutations [6–8]. It shows response rates of 10% to 27% in a broad NSCLC patient population after failure of chemotherapy [5].

Previously, we have shown surface-enhanced Raman spectroscopy (SERS) investigation of erlotinib immobilized onto potential silver colloidal nanocarriers [9]. These studies present vibrational spectroscopy characterization by means of Raman spectroscopy (RS) and Fourier-transform infrared absorption spectroscopy (FTIR) of the molecular structure of erlotinib in the solid state and solution in different pH conditions. These two complementary methods are commonly used for qualitative and quantitative analysis of different types of samples in various conditions and physical states [10–15]. RS and FTIR are governed by different quantum mechanical selection rules [16]. Mainly, vibrations that change polarizability of a molecule are active in RS spectra, while these which change molecular dipole moment are observed in FTIR spectra. Therefore, only the use of both spectroscopic methods provides comprehensive analysis of the investigated molecular structure. Additionally, by means of the density functional theory (DFT) calculations with the B3LYP hybrid theory level, the optimized geometry, wavenumber, and intensity of the vibrational bands of the investigated drug are provided. Such calculation method provides very good agreement between the calculated spectra and the corresponding experimental spectra of many molecules [10, 17–20]. Since there are a lot of publications regarding biological activity of erlotinib [21] and its successful application in NSCLC therapy [22, 23], there are no reports describing the 3D structure of this drug in detail what determines its application. Many research data confirm

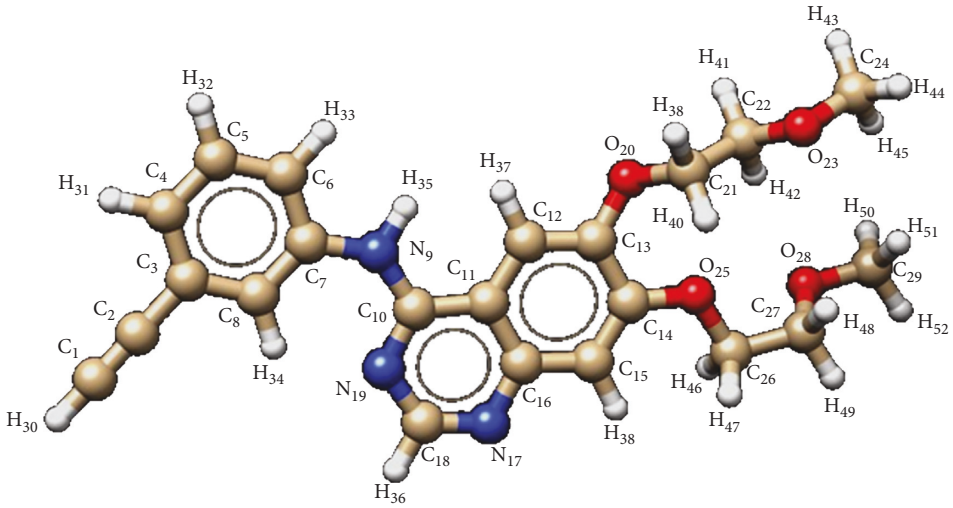

Figure 1: The optimized molecular structure of erlotinib drug [N-(3-ethynylphenyl)-6,7-bis (2-methoxyethoxy)-quinazolinamine hydrochloride].

that the compounds indicating similar chemical structure show different biological features [24, 25]. The spatial orientation of particular bonds determines therapeutic effect of the molecule. Deep knowledge and understanding of the molecular and geometric structure together with the recognized biological activity is important for developing new drug alternatives with more specific interaction or by improving the existing medical agents [26, 27]. Thus, the present study is crucial for better understanding the biological activity of erlotinib and for development of new tyrosine kinase inhibitors.

2. Materials and Methods

2.1. RS Measurements. The RS measurements for erlotinib were performed using the inVia Renishaw spectrometer combined with a CCD detector and confocal microscope Leica with the 20x magnification. The 532.8 nm laser wavelength with a 0.1% of the laser power was used as an excitation source. 3 scans were recorded in the range 2250–400 cm^{-1}, each with 30 s of the integration time and at 1 cm^{-1} spectral resolution.

2.2. FTIR Measurements. The FTIR experiments were performed using the vacuum VERTEX 70v FTIR Spectrometer for powder sample in the ATR mode with diamond crystal. The system is equipped with a KBr beamsplitter and a wide range DLaTGS detector. 128 scans were enough to acquire a good signal-to-noise ratio. The signal was collected in the range 2250–400 cm^{-1} at 1 cm^{-1} spectral resolution. Advanced ATR correction was applied for the spectrum before data analysis.

2.3. Theoretical Calculations. In order to optimize the ground-state geometry of the investigated drug and to obtain its theoretical vibrational spectra, the Gaussian 03 suite [28] with the density functional theory (DFT) method at the B3LYP theory level in vacuum and PCM model was employed. Such hybrid functional with 6-311G(d, p) basis set was successfully applied for calculations of similar molecules [18–20, 29]. During the optimization, no imaginary wavenumbers were observed. This implies that the optimized structures indicate energy minima on the potential energy surface for nuclear motion.

The theoretical Raman intensities were calculated using Raint software, which applied the following relationship [30]:

$$I_i = \frac{C(\nu_0 - \nu_i)^4 \cdot S_i}{\nu_i^{-1}\left[1 - \exp\left(-h\nu_i c/kT\right)\right]}, \quad (1)$$

where I_i is given in arbitrary units, C is a constant and equal to 10^{-12}, ν_0 is the wavenumber of laser excitation (cm^{-1}) (18768.8 cm^{-1} for 532.8 nm laser), ν_i is the DFT calculated frequency of the normal mode, S_i is the DFT calculated Raman scattering activity of the normal mode Q_i, T is the temperature (K), h is the Planck constant, and k is the Boltzmann constant.

The calculated RS and IR spectra were reproduced by the GaussSum 0.8 free software package [31]. For a better fit to the experimental vibrational bands, the theoretical wavenumbers were scaled using scaling factor of 0.991. The spectra were plotted with 11 cm^{-1} FWHM (full width at half maximum) and a 50%/50% Gaussian/Lorentzian band shape.

After comparison between the experimental and calculated spectral bands, some shortcomings can be observed. Such differentiation may result from conditions occurring in the experimental measurements and performed calculations. The RS and IR spectra were recorded for the sample in a solid state, while the DFT calculations were performed in vacuum. However, the obtained correlation is appropriate. On the other hand, the theoretical RS spectrum calculated in a PCM model corresponds very well with that measured in a solution.

Table 1: The selected calculated bond lengths and angles of erlotinib.

Bond	Bond length (Å)	Bonds	Angle (°)	Bonds	Dihedral angle (°)
C_1–C_2	1.204	C_2–C_3–C_8	119.5	C_6–C_7–N_9–C_{10}	−179.3
C_2–C_3	1.430	C_8–C_7–N_9	124.5	N_9–C_{10}–C_{11}–C_{12}	1.071
C_3–C_4	1.403	N_9–C_{10}–N_{19}	120.0	C_{11}–C_{12}–C_{13}–O_{20}	174.9
C_4–C_5	1.390	N_9–C_{10}–C_{11}	118.8	C_{16}–C_{15}–C_{14}–O_{25}	−179.1
C_5–C_6	1.388	C_{10}–C_{11}–C_{12}	125.8	C_{13}–O_{20}–C_{21}–C_{22}	131.2
C_6–C_7	1.405	C_{12}–C_{13}–O_{20}	118.5	O_{20}–C_{21}–C_{22}–O_{23}	177.6
C_7–C_8	1.398	C_{13}–O_{20}–C_{21}	119.2	C_{21}–C_{22}–O_{23}–C_{24}	−175.0
C_7–N_9	1.407	O_{20}–C_{21}–C_{22}	108.1	C_{14}–O_{25}–C_{26}–C_{27}	−179.6
N_9–C_{10}	1.372	C_{21}–C_{22}–O_{23}	107.0	O_{25}–C_{26}–C_{27}–O_{28}	−68.73
C_{10}–C_{11}	1.441	C_{22}–O_{23}–C_{24}	113.0	C_{26}–C_{27}–O_{28}–C_{29}	−176.8
C_{11}–C_{12}	1.414	C_{15}–C_{14}–O_{25}	125.0		
C_{12}–C_{13}	1.374	C_{14}–O_{25}–C_{26}	118.9		
C_{13}–C_{14}	1.433	O_{25}–C_{26}–C_{27}	108.4		
C_{14}–C_{15}	1.378	C_{26}–C_{27}–O_{28}	109.4		
C_{15}–C_{16}	1.414	C_{27}–O_{28}–C_{29}	112.8		
C_{16}–N_{17}	1.367				
N_{17}–C_{18}	1.310				
C_{18}–N_{19}	1.351				
N_{19}–C_{10}	1.323				
C_{11}–C_{16}	1.418				
C_{13}–O_{20}	1.364				
O_{20}–C_{21}	1.441				
C_{21}–C_{22}	1.519				
C_{22}–O_{23}	1.418				
O_{23}–C_{24}	1.412				
C_{14}–O_{25}	1.356				
O_{25}–C_{26}	1.428				
C_{26}–C_{27}	1.511				
C_{27}–O_{28}	1.412				
O_{28}–C_{29}	1.414				

3. Results and Discussion

3.1. Molecular Geometry. In order to identify the stable structure of erlotinib, twenty conformers were taken into consideration. Based on the differences between the calculated total energies of the examined conformers from DFT, the structure with the lowest energy was chosen for further analysis. Additionally, the theoretical RS and IR spectra of the selected conformer provide the best match to the experimental results. The bond lengths and angles of the optimized erlotinib structure obtained by means of the DFT/B3LYP method with 6-311G(d, p) basis set are given in Table 1, and the numbering of atoms is provided in Figure 1. The calculated value of the C≡C (C_1–C_2) bond which is 1.204 Å is comparable with the typical C≡C bond of the phenylacetylene (1.216 Å) [32, 33]. Similar observation occurs for the C_2–C_3 and C_3–C_4 bonds (see Figure 1), where for erlotinib, these distances are 1.430 Å and 1.403 Å, respectively. The corresponding bond lengths of the phenylacetylene molecule are equal to 1.448 Å and 1.395 Å, respectively [32]. In the case of the quinazoline moiety, which consisted of two fused aromatic rings, namely, benzene and pyrimidine rings, the C–N bonds indicate definitely shorter length in comparison with the corresponding bonds observed in the pyrimidine [34]. The C_{16}–N_{17}, N_{17}–C_{18}, C_{18}–N_{19}, and N_{19}–C_{10} bonds are equal to 1.367 Å, 1.310 Å, 1.351 Å, and 1.323 Å, respectively, while in the pyrimidine analogues [34], these bonds are 1.382 Å, 1.379 Å, 1.378 Å, and 1.374 Å, respectively. Also, the calculated angle bonds C_{16}–N_{17}–C_{18} and C_{18}–N_{19}–C_{10} (115.6° and 117.4°, respectively) differ from the corresponding angles of the pyrimidine [30], which are equivalent to 125.7° and 126.0°, respectively. On the other hand, the C–O bonds in the ethoxy moieties of the calculated erlotinib structure are almost the same length as the corresponding bonds in the ethoxy isomers [35, 36].

The C_{13}–O_{20}, C_{14}–O_{25} bonds and the O_{20}–C_{21}, O_{25}–C_{26} bonds are equal to 1.364 Å, 1.356 Å and 1.441 Å, 1.428 Å, respectively, while for the ethoxy benzaldehyde derivatives [32], these bonds are 1.359 Å and 1.433 Å, respectively. However, there are some differences for the C–O–C and O–C–C bond angles of erlotinib in comparison with those from the mentioned aromatic isomer [35]. The C_{13}–O_{20}–C_{21}, C_{14}–O_{25}–C_{26} bond angles and the O_{20}–C_{21}–C_{22}, O_{25}–C_{26}–C_{27} bond angles are equivalent to 119.2°, 118.9° and 108.1°, 108.4°. In the case of the corresponding bonds [35, 36], these angles are equal to 116.6° and 107.7°, respectively.

3.2. RS, FTIR, and DFT Studies. Figure 2 presents experimental and theoretical RS and FTIR spectra for the erlotinib drug in the spectral range of 2250–400 cm^{-1}. The theoretical

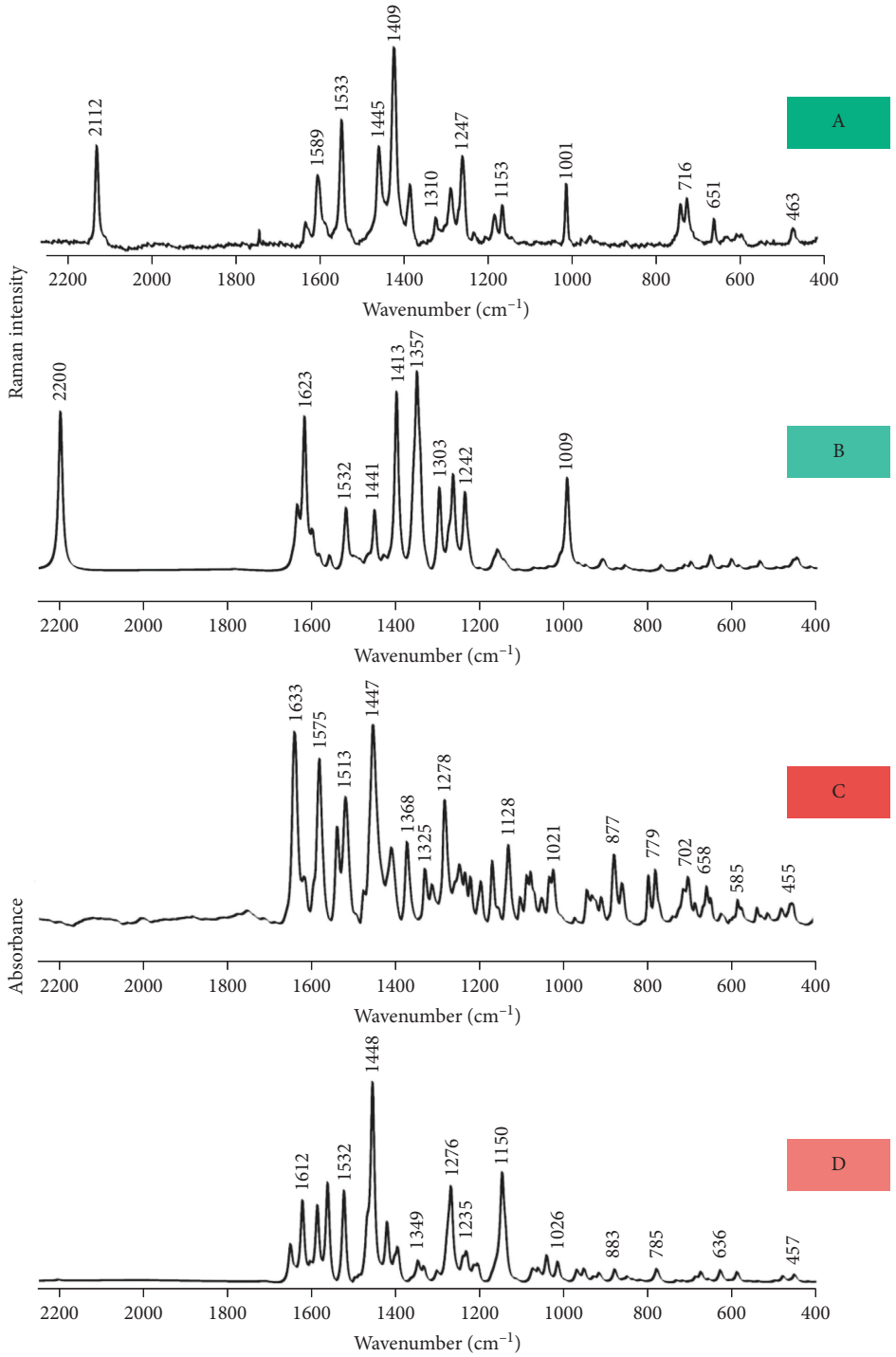

FIGURE 2: The experimental RS (A) and FTIR (C) spectra of erlotinib in the solid state together with the corresponding theoretical bands (B, RS; D, IR) calculated in the vacuum model in the spectral range of 2250–400 cm^{-1}.

wavenumbers, calculated at the DFT/B3LYP/6-311G(d, p) level in vacuum, demonstrate good correlation with the experimental bands. Moreover, the vibrational spectra for the aniline [37] and pyrimidine [38, 39] and RS spectra for phenylacetylene [40] and erlotinib [41, 42] were taken into consideration. All wavenumbers together with the appropriate assignments are listed in Table 2.

3.2.1. Aromatic Vibrations. As expected, the most intense RS bands are due to the vibrations of the phenylacetylene and quinazoline moieties (see Figure 2(a)). The bands assigned to the phenylacetylene ring modes, namely, $\nu(C{\equiv}C)$, $\nu(CC)_{Phe}$, $\rho_b(CH)_{Phe}$, $\delta(Phe)$, $\rho_{boop}(CH)_{Phe}$/$\delta_{oop}(Phe)$, $\rho_b(CH)_{C{\equiv}CH}$, $\delta_{oop}(Phe)$, and $\delta(Phe)$, are observed at 2112 cm^{-1}, 1572–1571 cm^{-1}, 1193–1179 cm^{-1},

Table 2: Calculated (vacuum) and experimental wavenumbers for the RS and FTIR spectra of erlotinib in the solid state.

Calculated wavenumbers (cm^{-1})	Assignment[a]		Experimental wavenumbers (cm^{-1})	
	B3LYP/6-311G(d, p) (PED > 5%)	Literature [9, 37–42]	RS	FTIR
2200	$\nu(C\equiv C)$		2112	
1623	$\nu(CC)_{Phe}$, $\rho_b(NH)$, $\nu(CN)_Q$		1619	1633
1612	$\nu(CC)_{Phe}$, $\rho_b(NH)$, $\nu(C=N)_Q$, $\nu(CC)_Q$	$\nu(CC)_Q$	1611	
1595	$\nu(CC)_Q$, $\nu(CN)_Q$, $\nu(CC)_{Phe}$	$\nu(CC)_{Phe}$	1589	
1571	$\rho_b(NH)$, $\nu(NC)_{Q\text{-}NH}$, $\nu(C=N)_Q$, $\nu(CC)_{C\Phi C}$, $\rho_b(CH)_{Phe}$, $\nu(CC)_Q$	$\nu(CC)_{Phe}$	1572	1575
1532	$\nu(CC)_Q$, $\rho_b(CH)_Q$, $\rho_s(CH_2)_{OCH2}$	ν(Phe), $\rho_b(NH)$	1533	
1518	$\rho_s(CH_2)_{CH2O}$, $\rho_s(CH_2)_{CH3}$			
1513	$\rho_s(CH_2)_{OCH2}$, $\rho_s(CH_2)_{CH3}$, $\rho_s(CH_2)_{CH2O}$		1514	1513
1441	$\rho_w(CH_2)_{CH2O}$, $\rho_w(CH_2)_{OCH2}$, $\rho_w(CH_3)$	$\rho_b(NH)$, ν(Phe)	1445	1447
1413	$\nu(C=N)_Q$, $\nu(CC)_Q$, $\rho_b(CH)_Q$, $\rho_b(NH)$	ν(Q), $\rho_b(NH)$, $\rho_b(CH)$	1409	1403
1373	$\rho_b(CH)_Q$, $\nu(CC)_Q$, $\rho_b(CH)_{Phe}$			
1364	$\rho_w(CH_2)_{CH2O}$, $\rho_w(CH_2)_{OCH2}$, $\rho_b(NH)$, $\rho_b(CH)_{Phe}$, $\nu(NC)_{Q\text{-}NH}$, $\nu(NC)_Q$		1372	1368
1303	$\rho_t(CH_2)_{CH2O}$, $\rho_t(CH_2)_{OCH2}$, $\rho_b(CH)_{Phe}$, $\nu(CC)_{Phe}$, $\nu(CN)_Q$, $\nu(CC)_Q$		1310	1309
1285	$\rho_b(CH)_{Phe\text{-}Q}$, $\nu(CC)_Q$, $\nu(NC)_Q$, $\rho_b(CH)_{Phe}$, $\nu(CC)_{Phe}$	ν(CN)	1275	1278
1242	$\rho_t(CH_2)_{OCH2}$, $\rho_t(CH_2)_{CH2O}$, $\rho_b(CH)_{Phe\text{-}Q}$, $\nu(CC)_Q$, $\nu(NC)_Q$, $\rho_b(CH)_{Phe}$, $\nu(CC)_{Phe}$	$\rho_b(CH)$, $\rho_b(NH)$, ν(CN)	1247	1243
1226	$\rho_w(CH_2)_{CH3}$, $\rho_t(CH_2)_{CH3}$, $\nu(CO)_{CH2O}$, $\rho_w(CH_2)_{CH2O}$			1230
1222	$\rho_w(CH_2)_{CH3}$, $\rho_t(CH_2)_{CH3}$, $\nu(CO)_{CH2O}$, $\rho_t(CH_2)_{OCH2}$, $\rho_w(CH_2)_{CH2O}$			
1215	$\rho_t(CH_2)_{OCH2}$, $\rho_t(CH_2)_{CH2O}$, $\nu(C_QO)$, δ(Q), $\rho_b(CH)_{Phe}$, δ(Phe)	ν(CN), $\delta_{(PYMD)}$	1219	1218
1179	$\rho_b(CH)_{Phe}$	$\rho_b(CH)$	1193	
1178	$\rho_w(CH_2)_{CH3}$, $\rho_t(CH_2)_{CH3}$			
1173	$\rho_w(CH_2)_{CH3}$, $\rho_t(CH_2)_{CH3}$, $\rho_b(CH)_{Phe}$, δ(Phe), $\rho_b(CH)_Q$, δ(Q), $\nu(C_QO)$	$\rho_b(CH)$, $\rho_b(CH)_{Phe}$	1170	1166
1158	$\rho_w(CH_2)_{CH3}$, $\rho_t(CH_2)_{CH3}$, $\nu(OC)_{OCH3}$, $\rho_t(CH_2)_{CH2O}$, $\rho_t(CH_2)_{OCH2}$			
1150	$\nu(OC)_{OCH3}$, $\rho_w(CH_2)_{CH3}$, $\rho_t(CH_2)_{CH3}$, $\rho_t(CH_2)_{CH2O}$, $\rho_t(CH_2)_{OCH2}$	$\nu_{as}(OCH_3)$, ν(COC)	1153	1152
1126	$\rho_t(CH_2)_{CH3}$, $\rho_t(CH_2)_{CH2O}$, $\rho_w(CH_2)_{CH3}$, $\rho_t(CH_2)_{CH3}$	δ(CH)		1128
1120	$\rho_b(CH)_{Phe}$, δ(Phe)			
1088	$\rho_b(CH)_Q$, δ(Q), $\rho_b(CH)_{Phe}$, $\nu(OC)_{OCH2}$			1099
1083	$\nu(CC)_{CH2\text{-}CH2}$, $\rho_w(CH_2)_{CH3}$, $\rho_t(CH_2)_{CH3}$			1083
1072	$\nu(OC)_{OCH2}$, $\rho_r(CH_2)$, $\rho_w(CH_2)_{CH3}$, $\rho_t(CH_2)_{CH3}$, δ(Q)			1075
1052	$\nu(CC)_{CH2\text{-}CH2}$, $\nu(OC)_{OCH3}$, $\rho_w(CH_2)$, $\rho_t(CH_2)$, $\rho_w(CH_2)_{CH3}$, $\rho_t(CH_2)_{CH3}$			1049
1026	$\nu(OC)_{OCH2}$, $\rho_b(CH)_{Phe\text{-}Q}$, $\nu(CO)_{CH2O}$, $\rho_w(CH_2)_{CH3}$, $\rho_t(CH_2)_{CH3}$			1021
1009	δ(Phe)	δ(Phe)	1001	1004
972	$\rho_{boop}(CH)_{Phe}$			970
941	$\rho_{boop}(CH)_{Phe}$		945	941
928	δ(Q), δ(Phe), $\delta(C_{Phe}NC_Q)$, $\rho_t(CH_2)$			929
922	δ(Q), $\rho_t(CH_2)$, $\nu(NC)_{Q\text{-}NH}$			921
891	$\rho_{boop}(CH)_{Phe\text{-}Q}$, δ_{oop}(Q), $\rho_{boop}(CH)_{Phe}$, δ_{oop}(Phe)			908
889	$\rho_{boop}(CH)_{Phe}$, δ_{oop}(Phe), $\rho_{boop}(CH)_{Phe\text{-}Q}$, δ_{oop}(Q)			
871	$\rho_r(CH_2)$, $\nu(OC)_{OCH3}$, $\nu(CO)_{CH2O}$, $\rho_{boop}(CH)_{Phe\text{-}Q}$, $\delta(C_QOC)$	$\rho_r(OC_2H_4)$		877
861	$\rho_{boop}(CH)_{Phe\text{-}Q}$, δ_{oop}(Phe-Q), $\delta(C_QOC)$, $\rho_r(CH_2)$, δ(PYMD-Q)		860	860
798	δ_{oop}(Q), $\rho_{boop}(CH)_{Phe\text{-}Q}$			796
791	$\rho_{boop}(CH)_{Phe}$, δ_{oop}(Phe)			
785	$\rho_{boop}(CH)_{Phe\text{-}Q}$, δ_{oop}(Q), $\delta(C_{Phe}NC_Q)$, $\delta(C_QOC)$, $\rho_r(CH_2)$, δ(Phe)			779
730	$\delta(C_{Phe}NC_Q)$, $\rho_{boop}(CH)_{Phe\text{-}Q}$, δ_{oop}(Phe-Q), $\delta(C_QOC)$, $\rho_r(CH_2)$, δ(PYMD-Q)	ρ_b(Q)	730	

Table 2: Continued.

Calculated wavenumbers (cm^{-1})	Assignment[a]		Experimental wavenumbers (cm^{-1})	
	B3LYP/6-311G(d, p) (PED > 5%)	Literature [9, 37–42]	RS	FTIR
715	$\rho_{boop}(CH)_{Phe\text{-}Q}$, δ_{oop}(Phe-Q), δ(PYMD-Q), $\rho_r(CH_2)$, $\delta(C_QOC)$, $\delta(C_{Phe}NC_Q)$, δ(Phe)		716	713
700	$\delta(C_QOC)$, $\rho_b(CH)_{Phe}$, δ(Phe)		702	702
687	$\rho_b(CH)_{C\equiv CH}$			686
669	δ(Q), δ(Phe), $\delta(C_QOC)$, $\rho_r(CH_2)$, $\delta(C_{Phe}NC_Q)$, $\rho_b(CH)_{C\equiv CH}$			
668	δ_{oop}(Q), $\delta_{oop}(C_{Phe}NC_Q)$, $\delta_{oop}(C_QOC)$, $\rho_b(CH)_{C\equiv CH}$, $\rho_r(CH_2)$	$\delta_{oop(PYMD)}$, δ(Phe)		658
641	$\rho_b(CH)_{C\equiv CH}$, $\rho_{boop}(CH)_{Phe}$, δ_{oop}(Phe)	δ(acetylene), δ(NH)	651	649
619	δ_{oop}(Phe), $\rho_b(CH)_{C\equiv CH}$, $\delta_{oop}(C_{Phe}NC_Q)$		623	624
601	δ(Phe), δ(Q), $\rho_b(CH)_{C\equiv CH}$	δ(Phe)	598	
574	$\rho_r(CH_2)$, δ(OCC), δ(Phe), δ(Q)		586	585
565	δ_{oop}(Q), $\rho_{boop}(CH)_{PYMD\text{-}Q}$, ρ_b(NH)			576
551	$\rho_b(CC)_{C\Phi C}$, δ(Phe), δ(Q)			540
512	$\rho_{boop}(CH)_{Phe\text{-}Q}$, δ_{oop}(Phe-Q), ρ_b(NH), $\delta_{oop}(C_QOC)$, δ_{oop}(OCC)			514
477	ρ_b(NH), $\rho_{boop}(CH)_{Phe}$, $\rho_{boop}(CC)_{C\Phi C}$, δ_{oop}(Phe)			482
465	ρ_b(NH), $\rho_{boop}(CH)_{Phe}$, $\rho_{boop}(CC)_{C\Phi C}$, δ_{oop}(Phe), δ_{oop}(Q), $\rho_{boop}(CH)_{PYMD\text{-}Q}$, $\delta(C_QOC)$, δ(CCO), δ(COC)			
462	δ(CCO), δ(COC), $\delta(C_QOC)$, δ(Q), ρ_b(NH)		463	455

[a]Abbreviations: ν, stretching; ρ_b, bending; ρ_w, wagging; ρ_s, scissoring; δ, deformation; as, antisymmetric; oop, out-of-plane; Phe, phenyl ring; *Q*, quinazoline group.

1170–1166 cm^{-1}, 1004–1001 cm^{-1}, 700–702 cm^{-1}, 651–641 cm^{-1}, 624–619 cm^{-1}, and 598 cm^{-1}, respectively (see Table 2). Some of these bands appear also in the corresponding FTIR spectrum (see Figure 2(c)). Additionally, the weak and medium intensity FTIR bands from the phenylacetylene vibrations are noticed at 972–970 cm^{-1} [$\rho_{boop}(CH)_{Phe}$], 941 cm^{-1} [$\rho_{boop}(CH)_{Phe}$], and 551–540 cm^{-1} [$\rho_b(CC)_{C\Phi C}$/δ(Phe)]. Moreover, the discussed aromatic ring modes indicate contribution to the bands observed at 586–574 cm^{-1} [δ(Phe)]. For the quinazoline moiety, the characteristic RS bands appear in the spectral ranges 1612–1611 cm^{-1}, 1595–1589 cm^{-1}, 1311–1303 cm^{-1}, 1247–1242 cm^{-1}, and 730–713 cm^{-1}. These spectral features are assigned to $\nu(CC)_Q$, $\nu(CN)_Q/\nu(CC)_Q$, and ρ_b(Q), respectively. There are also some bands due to the quinazoline vibrations appearing only in the FTIR spectrum, namely, the in-plane and out-of-plane deformation modes [δ(Q) and δ_{oop}(Q)] observed at 1099–1088 cm^{-1}, 929–921 cm^{-1}, 798–796 cm^{-1}, 668–658 cm^{-1}, and 576–565 cm^{-1}, respectively. However, it should be noticed that the considered aromatic moiety consists of two fused aromatic rings: phenyl and pyrimidine. Therefore, some spectral features associated with these aromatic rings separately can be distinguished. The main influence on the bands in the spectral ranges 730–713 cm^{-1} and 514–512 cm^{-1} indicates phenyl ring. The mentioned bands are assigned to the $\rho_{boop}(CH)_{Phe\text{-}Q}/\delta_{oop}$(Phe-Q) vibrations. In the case of the pyrimidine moiety of the quinazoline, the stronger contribution to the bands at 1413–1403 cm^{-1} and 1219–1215 cm^{-1} attributed to the $\nu(C{=}N)_Q$ and δ(PYMD)/$\nu(C_QO)$ modes, respectively, is observed.

3.2.2. Aliphatic Vibrations. The presence of the methoxy and ethoxy groups is manifested by the several characteristic RS and FTIR spectral features (see Figure 2). These bands appear in the spectral ranges 1514–1513 cm^{-1}, 1230–1222 cm^{-1}, 1128–1126 cm^{-1}, 1083 cm^{-1}, 1075–1072 cm^{-1}, 1052–1049 cm^{-1}, 877–871 cm^{-1}, and 463–455 cm^{-1} and correspond to the $\rho_s(CH_2)_{OCH2}/\rho_s(CH_2)_{CH3}/\rho_s(CH_2)_{CH2O}$, $\rho_{w/t}(CH_2)_{CH3}/\nu(CO)_{CH2O}$, δ(CH), $\nu(CC)_{CH2\text{-}CH2}/\rho_w(CH_2)_{CH3}$, $\nu(OC)_{OCH2}/\rho_r(CH_2)$, $\nu(CC)_{CH2\text{-}CH2}/\nu(OC)_{OCH3}$, $\rho_r(OC_2H_4)$, and δ(CCO)/δ(COC) vibrations, respectively. In the case of the amino moiety, the strong and medium intensity bands due to the ρ_b(NH) and ν(CN) modes occur in the spectral ranges 1534–1532 cm^{-1}, 1447–1441 cm^{-1}, and 1278–1275 cm^{-1}, respectively. Additionally, this functional group indicates contribution to the spectral features at 1413–1403 cm^{-1} and 1372–1364 cm^{-1} assigned to the ρ_b(NH) mode.

3.2.3. pH-dependent RS Studies. Due to the possible protonation occurring for the amino and quinazoline moieties of erlotinib, the RS experiments in various pH conditions were performed. Figure 3 presents the RS spectra of the investigated drug at pH between 3 and 11 in the spectral range of 2250–400 cm^{-1}. Additionally, the calculations at the DFT/B3LYP/6-311G(d, p) level in PCM model were performed. The theoretical RS spectrum correlates very well with the corresponding RS spectrum measured for the investigated drug at pH = 7 (see Figure 3). Table 3 lists the wavenumbers and the appropriate band assignments. The obtained vibrational data indicate almost the same spectral pattern; however, some relative intensity changes become

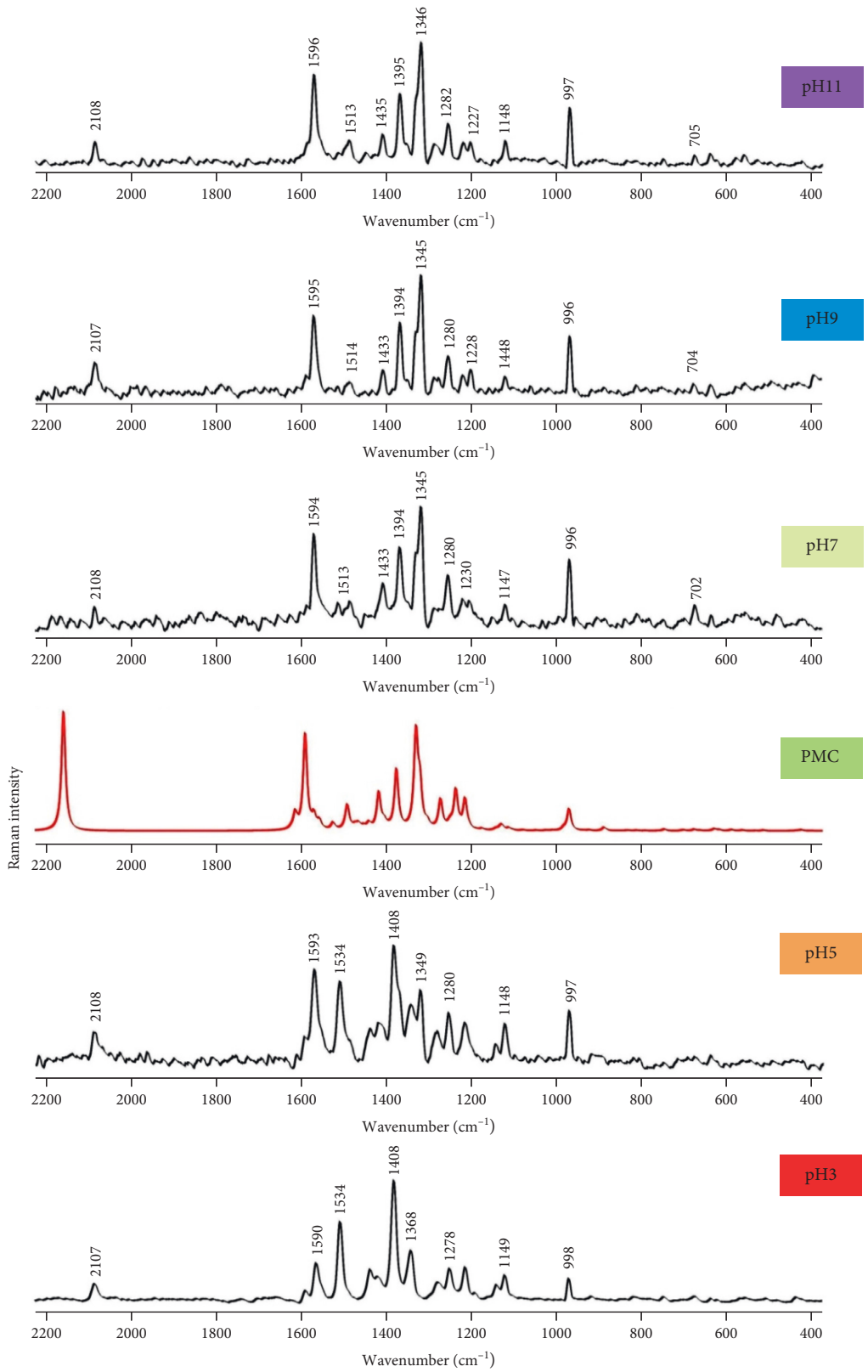

Figure 3: The RS spectra of erlotinib at pH conditions between 3 and 11 (black lines) in the spectral range of 2250–400 cm^{-1} together with the theoretical bands calculated in the PCM model (red line).

Table 3: Calculated (PCM model) and experimental wavenumbers for the RS spectra of erlotinib in the solution (pH 7).

Calculated wavenumbers (cm^{-1})	Assignment[a]	Experimental wavenumbers (cm^{-1})	
	B3LYP/6-311G(d, p) (PED > 5%)	Literature [9, 37–42]	RS
2184	ν(C≡C)		2108
1606	$\nu(CC)_{Phe}$, $\rho_b(NH)$, $\nu(C{=}N)_Q$, $\nu(CC)_Q$	$\nu(CC)_Q$	1594
1541	$\rho_b(NH)$, $\nu(NC)_{Q\text{-}NH}$, $\nu(CN)_Q$, $\nu(C{=}N)_Q$, $\rho_b(CH)_{Phe}$, $\nu(CC)_Q$	ν(Phe), $\rho_b(NH)$	1539
1517	$\nu(CC)_Q$, $\rho_s(CH_2)_{OCH2}$, $\rho_s(CH_2)_{CH3}$		1513
1440	$\nu(CC)_{Phe}$, $\rho_b(CH)_{Phe}$, $\nu(NC)_{Q\text{-}NH}$,	$\rho_b(NH)$, ν(Phe)	1433
1399	$\nu(C{=}N)_Q$, $\nu(CC)_Q$, $\rho_b(CH)_Q$, $\rho_b(NH)$	ν(Q), $\rho_b(NH)$, $\rho_b(CH)$	1394
1355	$\rho_b(CH)_Q$, $\nu(CC)_Q$, $\rho_b(CH)_{Phe}$		1357
1346	$\rho_w(CH_2)_{CH2O}$, $\rho_w(CH_2)_{OCH2}$, $\rho_w(CH_3)$, $\nu(CC)_Q$, $\nu(CN)_Q$,		1345
1298	$\rho_b(CH)_{Phe}$, $\nu(CC)_{Phe}$, $\rho_w(CH_2)_{CH2O}$, $\rho_w(CH_2)_{OCH2}$, $\rho_b(CH)_{Phe\text{-}Q}$, $\nu(CC)_Q$, $\nu(NC)_Q$	ν(CN)	1280
1266	$\rho_t(CH_2)_{OCH2}$, $\rho_t(CH_2)_{CH2O}$, $\rho_b(CH)_{Phe\text{-}Q}$, $\nu(CC)_Q$, $\nu(NC)_Q$, $\rho_b(CH)_{Phe}$, $\nu(CC)_{Phe}$	$\rho_b(CH)$, $\rho_b(NH)$, ν(CN)	1246
1240	$\rho_w(CH_2)_{CH3}$, $\rho_t(CH_2)_{CH3}$, $\nu(CO)_{CH2O}$, $\rho_w(CH_2)_{CH2O}$, $\rho_b(CH)_{Phe}$, $\rho_b(CH)_Q$		1230
1144	$\rho_b(CH)_{Phe}$, $\rho_b(CH)_{Phe\text{-}Q}$, $\rho_w(CH_2)_{CH3}$		1147
998	δ(Phe)	δ(Phe)	996
703	δ_{oop}(Phe-Q), δ(PYMD-Q), $\delta(C_QOC)$, $\rho_b(CH)_{Phe}$, δ(Phe), $\rho_s(CH_2)_{CH2O}$, $\rho_s(CH_2)_{OCH2}$		702

[a]Abbreviations: ν, stretching; ρ_b, bending; ρ_w, wagging; ρ_s, scissoring; δ, deformation; as, antisymmetric; oop, out-of-plane; Phe, phenyl ring; Q, quinazoline group.

noticeable upon different pH values, and they prove the presence of protonated structures. The RS spectra of erlotinib collected in the acidic environment show strong and medium intensity bands due to the amino group vibrations, namely, ~1534 cm^{-1}, ~1464 cm^{-1}, ~1368 cm^{-1}, and ~1280 cm^{-1} associated with the ρ_b(NH) and ν(CN) modes, respectively (see Tables 2 and 3). Nevertheless, together with the pH increasing from 7 to 11, the crucial weakening of the band intensities especially related to the ρb(NH) vibrations is observed (see Figure 3). According to the literature, the erlotinib dissociation constant is equal to 5.4 [43]; thus, the spectral patterns discussed above should be the result of the $-NH^+$ presence in the acidic medium and its absence in the neutral and alkaline environments. In the case of quinazoline, the observed spectral variations suggest that the protonation for this moiety may also occur. The strong and medium intensity bands at ~1408 cm^{-1} [$\nu(C{=}N)_Q$] and ~1308 cm^{-1} [$\nu(CC)_Q$]/$\nu(CN)_Q$] and ~1241 cm^{-1} [$\nu(CC)_Q$]/$\nu(CN)_Q$] in the RS spectra for erlotinib at pH equal to 3 and 5 indicate significant weakening and shift to ~1394 cm^{-1} and ~1311 cm^{-1} and ~1246 cm^{-1}, respectively, when the pH rises above 7 (see Figure 3). Such phenomenon may support the statement that in the acidic medium, the protonated $C{=}N^+$ form occurs. This is also confirmed by the noticed blue shift for the band assigned to $\nu(CC)_{Phe\text{-}Q}$ from ~1590 cm^{-1} (pH = 3) to ~1596 cm^{-1} (pH = 11) upon pH values increasing (see Figure 3). This spectral feature has been already considered as a pH-sensitive band [44]. Furthermore, in the RS spectrum for erlotinib at pH = 5 appear bands associated with the ethoxy group vibrations. The mentioned bands are visible at ~1513 cm^{-1} and ~1345 cm^{-1}, and they are assigned to the $\rho_s(CH_2)$ and $\rho_w(CH_2)$, respectively. Intensity of these bands becomes stronger upon pH increasing. Moreover, in the neutral and alkaline environments, bands at ~1230 cm^{-1} and ~702 cm^{-1} occur due to the $\rho_{w/t}(CH_2)CH_3/\nu(CO)_{CH2O}$ and $\delta(C_QOC)$ modes.

4. Conclusions

In this study, we performed the first characterization of vibrational structure of erlotinib, a drug approved in NSCLC therapy, based on RS and FTIR spectroscopies in solid state and solution in different pH conditions. Additionally, the optimized molecular structure of erlotinib was elucidated in detail based on the experimental data, which were supported by DFT/6-311G(d, p) calculations. Simultaneously, the performed RS measurements for the investigated drug in different pH conditions show that in the acidic environment, the protonated $-NH^+$ and $C{=}N^+$ forms occur.

Data Availability

The data used to support the findings of this study are available from the corresponding author upon request.

Conflicts of Interest

The authors declare that there are no conflicts of interest.

Acknowledgments

This study was supported by the National Science Centre Poland (grant no. 2016/21/D/ST4/02178 to N.P.).This research was performed using equipment purchased in the frame of the project cofunded by the Małopolska Regional Operational Program Measure 5.1 Krakow Metropolitan Area as an important hub of the European Research Area for

2007–2013, project no. MRPO.05.01.00-12-013/15. The authors kindly acknowledge the PL-Grid Infrastructure (Academic Computer Center "Cyfronet" in Krakow) for computational facilities.

References

[1] K. R. Loeb and L. A. Loeb, "Significance of multiple mutations in cancer," *Carcinogenesis*, vol. 21, no. 3, pp. 379–385, 2000.

[2] C. C. Cortez and P. A. Jones, "Chromatin, cancer and drug therapies," *Mutation Research*, vol. 647, no. 1-2, pp. 44–51, 2008.

[3] S. Sarkar, G. Horn, K. Moulton et al., "Cancer development, progression, and therapy: an epigenetic overview," *International Journal of Molecular Sciences*, vol. 14, no. 10, pp. 21087–21113, 2013.

[4] G. Samara, M. Hurwitz, M. Sawicki, and E. Passaro Jr., "Molecular mechanisms of tumor formation," *The American Journal of Surgery*, vol. 164, no. 4, pp. 389–396, 1992.

[5] S. T. Kim, J. Lee, J.-H. Kim et al., "Comparison of gefitinib versus erlotinib in patients with nonsmall cell lung cancer who failed previous chemotherapy," *Cancer*, vol. 116, no. 12, pp. 3025–3033, 2010.

[6] Q. Dai, Y.-H. Ling, M. Lia et al., "Enhanced sensitivity to the HER1/epidermal growth factor receptor tyrosine kinase inhibitor erlotinib hydrochloride in chemotherapy-resistant tumor cell lines," *Clinical Cancer Research*, vol. 11, no. 4, pp. 1572–1578, 2005.

[7] J. Smith, "Erlotinib: small-molecule targeted therapy in the treatmentof non-small-cell lung cancer," *Clinical Therapeutics*, vol. 27, no. 10, pp. 1513–1534, 2005.

[8] F. Passiglia, A. Listì, M. Castiglia et al., "EGFR inhibition in NSCLC: new findings. . .. and opened questions?," *Critical Reviews in Oncology/Hematology*, vol. 112, pp. 126–135, 2017.

[9] N. Piergies, M. Oćwieja, C. Paluszkiewicz, and W. M. Kwiatek, "Identification of erlotinib adsorption pattern onto silver nanoparticles: SERS studies," *Journal of Raman Spectroscopy*, vol. 49, no. 8, pp. 1265–1273, 2018.

[10] H. Domin, E. Pięta, N. Piergies et al., "Neuropeptide Y and its C-terminal fragments acting on Y 2 receptor: Raman and SERS spectroscopy studies," *Journal of Colloid and Interface Science*, vol. 437, no. 1, pp. 111–118, 2015.

[11] X. Zhang, L. Chen, Y. Bai, and K. Chen, "Study on the processing technology of calamine calcination by near-infrared spectroscopy," *Journal of Spectroscopy*, vol. 2019, Article ID 9326789, 13 pages, 2019.

[12] T. Ö. Öge, "FT-IR, laser-Raman, UV-Vis, and NMR spectroscopic studies of antidiabetic molecule nateglinide," *Journal of Spectroscopy*, vol. 2018, Article ID 8573014, 12 pages, 2018.

[13] C. Paluszkiewicz, N. Piergies, A. Sozańska et al., "Vibrational microspectroscopy analysis of human lenses," *Spectrochimica Acta Part A: Molecular and Biomolecular Spectroscopy*, vol. 188, no. 5, pp. 332–337, 2018.

[14] E. Pięta, J. Lekki, J. M. del Hoyo Melendez et al., "Surface characterization of medieval silver coins minted by the early piasts: FT-IR mapping and SEM/EDX studies," *Surface and Interface Analysis*, vol. 50, no. 1, pp. 78–86, 2018.

[15] R. Legner, A. Wirtz, and M. Jaeger, "Using compact 1H NMR, NIR, and Raman spectroscopy combined with multivariate data analysis to monitor a biocatalyzed reaction in a microreaction system," *Journal of Spectroscopy*, vol. 2018, p. 11, 2018.

[16] M. Urban and C. D. Craver, *Structure-Property Relations in Polymers*, American Chemical Society, Washington, DC, USA, 1993.

[17] M. Pagliai, I. Osticioli, A. Nevin, S. Siano, G. Cardini, and V. Schettino, "DFT calculations of the IR and Raman spectra of anthraquinone dyes and lakes," *Journal of Raman Spectroscopy*, vol. 49, no. 4, pp. 668–683, 2018.

[18] N. Piergies, E. Proniewicz, A. Kudelski et al., "Fourier transform infrared and Raman and surface-enhanced Raman spectroscopy studies of a novel group of boron analogues of aminophosphonic acids," *The Journal of Physical Chemistry A*, vol. 116, no. 40, pp. 10004–10014, 2012.

[19] N. Piergies, E. Proniewicz, Y. Ozaki, Y. Kim, and L. M. Proniewicz, "Influence of substituent type and position on the adsorption mechanism of phenylboronic acids: infrared, Raman, and surface-enhanced Raman spectroscopy studies," *The Journal of Physical Chemistry A*, vol. 117, no. 27, pp. 5693–5705, 2013.

[20] N. Piergies and E. Proniewicz, "Structure characterization of [N-Phenylamino(2-boronphenyl)-R-methyl]phosphonic acid by vibrational spectroscopy and density functional theory calculations," *Journal of Spectroscopy*, vol. 2014, Article ID 247237, 8 pages, 2014.

[21] J. Dowell, J. D. Minna, and P. Kirkpatrick, "Erlotinib hydrochloride," *Nature Reviews Drug Discovery*, vol. 4, no. 1, pp. 13-14, 2005.

[22] C. M. Rocha-Lima and L. E. Raez, "Erlotinib (tarceva) for the treatment of non–small-cell lung cancer and pancreatic cancer," *Drug Review*, vol. 34, no. 10, pp. 554–564, 2009.

[23] D. Rossi, D. Dennetta, M. Ugolini et al., "Activity and safety of erlotinib as second- and third-line treatment in elderly patients with advanced non-small cell lung cancer: a phase II trial," *Targeted Oncology*, vol. 5, no. 4, pp. 231–235, 2010.

[24] H. Kubinyi, "Chemical similarity and biological activities," *Journal of the Brazilian Chemical Society*, vol. 13, no. 6, pp. 717–726, 2002.

[25] N. Chhabra, M. Aseri, and D. Padmanabhan, "A review of drug isomerism and its significance," *International Journal of Applied and Basic Medical Research*, vol. 3, no. 1, pp. 16–18, 2013.

[26] I. Ukrainets, G. Hamza, A. Burian et al., "Molecular conformations and biological activity of N-Hetaryl(aryl)alkyl-4-methyl-2,2-dioxo-1H-2λ^6, 1-benzothiazine-3-carboxamides," *Scientia Pharmaceutica*, vol. 86, no. 50, pp. 1–27, 2018.

[27] H. A. Abdel-Aziz, H. A. Ghabbour, W. M. Eldehna, M. M. Qabeel, and H. K. Fun, "Synthesis, crystal structure, and biological activity of cis/trans amide rotomers of (Z)-N'-(2-Oxoindolin-3-ylidene)formohydrazide," *Journal of Chemistry*, vol. 2014, Article ID 760434, 7 pages, 2014.

[28] M. J. Frisch, G. W. Trucks, H. B. Schlegel et al., *Gaussian03, Revision A.1*, Gaussian Inc., Pittsburgh, PA, USA, 2003.

[29] E. Pięta, N. Piergies, M. Oćwieja et al., "Monitoring the interfacial behavior of selective Y5 receptor antagonist on colloidal gold nanoparticle surfaces: surface-enhanced vibrational spectroscopy studies," *The Journal of Physical Chemistry C*, vol. 121, no. 32, pp. 17276–17288, 2017.

[30] D. Michalska and R. Wysokiński, "The prediction of Raman spectra of platinum(II) anticancer drugs by density functional theory," *Chemical Physics Letters*, vol. 403, no. 1–3, pp. 211–217, 2005.

[31] N. M. O'Boyle and J. G. Vos, *GaussSum 0.8*, Dublin City University, Dublin, 2004, http://gausssum.sourceforge.net.

[32] Y. Amatatsu and Y. Hasebe, "Ab initio study on phenylacetylene in S1 and S2," *The Journal of Physical Chemistry A*, vol. 107, no. 50, pp. 11169–11173, 2003.

[33] G. N. Patwari, P. Venuvanalingam, and M. Kołaski, "Phenylacetylene dimer: ab initio and DFT study," *Chemical Physics*, vol. 415, pp. 150–155, 2013.

[34] A. Barakat, H. J. Al-Najjar, A. M. Al-Majid et al., "Synthesis, NMR, FT-IR, X-ray structural characterization, DFT analysis and isomerism aspects of 5-(2,6-dichlorobenzylidene)pyrimidine-2,4,6(1H,3H,5H)-trione," *Spectrochimica Acta Part A: Molecular and Biomolecular Spectroscopy*, vol. 147, pp. 107–116, 2015.

[35] T. Chithambarathanu, K. Vanaja, and J. D. Magdaline, "Molecular structure, spectroscopic studies, homo-lumo profile and nbo analysis of 3-ethoxy-4-hydroxy benzaldehyde," *Rasayan Journal of Chemistry*, vol. 8, no. 4, pp. 490–508, 2015.

[36] F. Anam, A. Abbas, K. M. Lo et al., "Synthesis, crystal structure, experimental and theoretical investigations of 3-(4-ethoxy-3-methoxyphenyl)-1-phenylprop-2-en-1-one," *Journal of Molecular Structure*, vol. 1127, pp. 472–750, 2017.

[37] Y. Qi, Y. Hu, M. Xie, D. Xing, and H. Gu, "Adsorption of aniline on silver mirror studied by surface-enhanced Raman scattering spectroscopy and density functional theory calculations," *Journal of Raman Spectroscopy*, vol. 42, no. 6, pp. 1287–1293, 2011.

[38] R. Dornhaus, M. B. Long, R. E. Benner, and R. K. Chang, "Time development of SERS from pyridine, pyrimidine, pyrazine, and cyanide adsorbed on ag electrodes during an oxidation-reduction cycle," *Surface Science*, vol. 93, no. 1, pp. 240–262, 1980.

[39] M. Muniz-Miranda, N. Neto, and G. Sbrana, "Surface-enhanced Raman spectra of pyrazine, pyrimidine, and pyridazine adsorbed on silver sols," *The Journal of Physical Chemistry*, vol. 92, no. 4, pp. 954–959, 1988.

[40] T. W. Lee, K. Kim, and M. S. Kim, "Raman spectroscopy of phenylacetylene adsorbed on silver surfaces," *Journal of Molecular Structure*, vol. 274, pp. 59–73, 1992.

[41] A. T. N. Lam, J. Yoon, E.-O. Ganbold et al., "Adsorption and desorption of tyrosine kinase inhibitor erlotinib on gold nanoparticles," *Journal of Colloid and Interface Science*, vol. 425, pp. 96–101, 2014.

[42] S. F. El-Mashtoly, D. Petersen, H. K. Yosef et al., "Label-free imaging of drug distribution and metabolism in colon cancer cells by Raman microscopy," *The Analyst*, vol. 139, no. 5, pp. 1155–1161, 2014.

[43] K. Miyazaki, S. Sato, T. Kodama et al., "Effect of acid suppressants on the efficacy of tyrosine kinase inhibitors in patients with epidermal growth factor receptor-mutated non-small-cell lung cancer," *Molecular and Clinical Oncology*, vol. 4, no. 5, pp. 873–877, 2016.

[44] N. Wattanavichean, E. Casey, R. J. Nichols, and H. Arnolds, "Discrimination between hydrogen bonding and protonation in the spectra of a surface-enhanced Raman sensor," *Physical Chemistry Chemical Physics*, vol. 20, no. 2, pp. 866–871, 2018.